ADVANCED FUNCTIONAL MATERIALS
www.afm-journal.de

Highly Efficient Blue Light-Emitting Diodes Based on Perovskite Film with Vertically Graded Bandgap and Organic Grain Boundary Passivation Shells

*Lei Shu, Bing Han, Qianpeng Zhang, Swapnadeep Poddar, Daquan Zhang, Yu Fu, Yang-Bryan Cao, Yucheng Ding, Yudong Zhu, Yuanjing Lin, Dai-Bin Kuang, Jin-Feng Liao, and Zhiyong Fan**

Metal halide perovskite materials have emerged as a promising class of semiconductors for high-performance optoelectronic applications, particularly for light-emitting diodes (LEDs), due to their high quantum efficiency, facile color tunability, narrow emission line widths, as well as cost-effectiveness. Despite the great successes on green and red perovskite LEDs (PeLEDs), the external quantum efficiency (EQE) of blue PeLEDs still lags far behind that of green and red counterparts. Here, wavelength tunable pure and deep blue PeLEDs with high EQE are presented, achieving 17.5% and 10.8% for emission wavelengths of 472 and 461 nm, respectively. The wavelength tenability and high EQE are attributed to the unique vertically graded bandgaps and grain boundary organic shells in the perovskite films. The results demonstrate a significant performance improvement in blue PeLEDs, provide a novel route to fabricate high-performance pure and deep blue PeLEDs that can match the performance of the green and red PeLEDs for future lighting and display applications.

1. Introduction

Blue light-emitting diodes (LEDs) are critical components in solid-state lighting and full-color displays, but developing blue PeLEDs with an emission wavelength shorter than 475 nm is particularly challenging.[1–8] While PeLEDs with emission wavelength from near infrared to green have achieved EQEs above 20%,[7–12] the performance of blue PeLEDs still lags far behind because blue emissive perovskite materials usually are plagued by deficient stability and quantum efficiency.[13] Previous literature have reported two primary strategies for developing blue PeLEDs, namely, perovskite compositional tuning and quantum confinement (QC) engineering.[13] By tuning the ratio of halides, mostly Cl and Br, in the perovskite nanocrystals, emission from deep blue to green can be realized. For example, blue (477 nm) and deep blue (467 nm) LEDs based on the mixed halide three-dimensional (3D) perovskites with modest EQE values of 11% and 5.5% were realized by using a vapor-assisted crystallization technique, generating the 3D perovskites with compositional homogeneity.[14] However, the local compositional heterogeneity of mixed halides in lead octahedrons produces ionic defects, leading to ion migration and phase segregation, and consequently results in the redshift of the emission spectrum under electrical bias or light illumination.[15] In parallel, reduced dimensional (e.g., quasi-2D) perovskite materials are being explored to realize blue emission by inserting organic ammonium ligand as a spacer in between 2D inorganic octahedron lattice layers to convert the 3D bulk perovskite into a 2D composite material.[16,17] In this scenario, each 2D lattice layer provides a QC effect for carriers, thus leading to widened energy bandgap (E_g). And the overall E_g of a low-dimensional domain is determined by the number of constituent lattice layers (n) stacking up without ligands. For example, for the $CsPbBr_3$-based quasi-2D perovskites, in principle the E_g can be tuned from about 2.6 eV ($n = 4$, $\lambda = 477$ nm) to 2.7 eV ($n = 3$, $\lambda = 460$ nm), 2.9 eV ($n = 2$, $\lambda = 427$ nm), and 3.1 eV ($n = 1$, $\lambda = 400$ nm) respectively, by reducing the number of the octahedron layers.[2–18] For previously

L. Shu, Q. Zhang, S. Poddar, D. Zhang, Y. Fu, Y.-B. Cao, Y. Ding, Z. Fan
Department of Electronic and Computer Engineering
The Hong Kong University of Science and Technology
Clear Water Bay, Kowloon, Hong Kong SAR China
E-mail: eezfan@ust.hk
B. Han, Y. Zhu, Y. Lin
Department of Materials Science and Engineering
Southern University of Science and Technology
Shenzhen, Guangdong 518055, China
D.-B. Kuang, J.-F. Liao
MOE Key Laboratory of Bioinorganic and Synthetic Chemistry
Lehn Institute of Functional Materials
School of Chemistry
Sun Yat
sen University
Guangzhou 510275, China
Z. Fan
Guangdong-Hong Kong-Macao Intelligent Micro-Nano Optoelectronic Technology Joint Laboratory
The Hong Kong University of Science and Technology
Clear Water Bay, Kowloon, Hong Kong SAR China

The ORCID identification number(s) for the author(s) of this article can be found under https://doi.org/10.1002/adfm.202306570

DOI: 10.1002/adfm.202306570

reported quasi-2D perovskite films, an inhomogeneous energy landscape consists of multiple *n* value phases.[19] Accordingly, by cascade energy transfer process, the energy is channeled across the inhomogeneous energy landscape, guiding carriers to the lowest bandgap *n* phase which improves the emission efficiency. However, because carriers are guided to the lowest bandgap *n* phase, even there are larger bandgap *n* phases in quasi-2D perovskite films, thus only long wavelength emission such as sky-blue emission can be achieved.[18–20] Therefore, it is still challenging to achieve pure blue or deep blue emissions based on quasi-2D perovskite materials.

To address this challenge, in this report, we demonstrate a highly efficient blue PeLED based on a unique perovskite material ($PDACs_{n-1}Pb_n(Br_{0.77}Cl_{0.37})_{3n+1}$) with vertically graded bandgap and organic grain boundary passivation shells. Herein, the short length organic ligand propane-1,3-diammonium bromide ($PDABr_2$) is used to improve the carrier transfer between various *n* phases to improve the carrier injection efficiency. The $PbCl_2$ is doped into the perovskite precursor solution to extend the distribution of PDA^{2+} cations to rearrange the distribution of various *n* phases in the films thus forming a vertically graded bandgap structure and grain boundary organic shells. In addition, the $PbCl_2$ can stabilize the precursor phase and slow down the crystallization process of perovskite.[21] Under the synergetic effect of $PbCl_2$ and PDA^{2+} cations, the perovskite materials with vertically graded bandgap and grain boundary organic shells can be obtained by the self-regulation of the reduced-dimensional perovskite during the annealing process. Due to the unique vertically graded bandgap *n* phase in quasi-2D perovskite films, the lateral bandgap variation at the recombination zone is small enough to hinder the cascade energy transfer to achieve pure and deep blue emission. At the same time, the grain boundary organic shells can effectively passivate the boundary defects to improve the device performance.[9]

As a result, the tunable wavelength of pure blue (472 nm) and deep blue (461 nm) ELs are achieved with the record high EQE values of 17.5% and 10.8%, respectively. Our work demonstrates the alluring potency to use well-engineered quasi-2D perovskites for high-performance PeLEDs and highlights the importance of controlling the distribution of low-dimensional structures as well as the organic grain boundary passivation shells inside the material.

2. Results and Discussion

In this work, we synthesized $PDACs_{n-1}Pb_n(Br_{0.55}Cl_{0.37})_{3n+1}$ using $PDABr_2$, cesium bromide (CsBr), lead chloride ($PbCl_2$), and lead bromide ($PbBr_2$) with molar ratios of 0.17: 0.31: 0.18: 0.12 are used to form. We found that doping Cl can extend the distribution of organic ligands in the perovskite film, as shown in **Figure 1**a. The atomic concentration depth analysis by Kratos X-ray photoelectron spectrometer (Axis Ultra DLD by Kratos) on perovskite films with 0.0:1.0 and 0.6:0.4 $PbCl_2$ to $PbBr_2$ molar ratios are shown in Figure S1a,b (Supporting Information), respectively. For perovskite film without Cl doping (0.0:1.0 molar ratio), the distribution of N element (from the organic ligand $PDABr_2$) has a relatively shallow depth, indicating the presence of quasi-2D component comprising $PDABr_2$, specifically close to the upper surface of the film, as shown in Figure S1a (Supporting Information). After introducing $PbCl_2$ into perovskite materials, the distribution depth of N element is significantly increased, as shown in Figure S1b (Supporting Information). Although the N element concentration also experiences a fast decay with increase of depth, it possesses a long tail, as shown in Figure S1b (Supporting Information). On the other hand, the morphology of the perovskite film is also significantly improved after Cl doping. The scanning electron microscope (SEM) and atomic force microscopy (AFM) are used to characterize the morphology of the perovskite thin films, as shown in Figures S2 and S3 (Supporting Information). For the pure bromide perovskite film, there are some pinholes on the film, as shown in Figure S2a (Supporting Information). After optimizing the molar ratio of $PbCl_2$ over $PbBr_2$ to 0.6: 0.4, the pinhole-free perovskite film with uniform crystal size is formed, as shown in Figure S2b (Supporting Information). In addition, when the molar ratio of $PbCl_2$ to $PbBr_2$ is increased to 1.0: 0.0, the pinholes in the perovskite film re-appear (in Figure S2c, Supporting Information), and it was observed that the grain size in Figure S2c (Supporting Information) is much larger than that in Figure S2a (Supporting Information).

Here, the perovskite films with vertically graded bandgap and grain boundary organic shells are formed, as shown in Figure S1b (Supporting Information). By controlling the Cl doping, a graded distribution of PDA2+ cations in perovskite film can be obtained, which leads to the formation of the vertically graded bandgaps and grain boundary organic shells. The distribution of reduced-dimensional quasi-2D perovskite in film is controlled by the intercalating cation, stoichiometry of the precursor, and the deposition process (such as annealing).[22,23] In order to further investigate the interaction between PDA2+ organic cations and perovskite after Cl doping, we further performed X-ray photoelectron spectroscopy (XPS). The affinity between the PDA2+ cation and the perovskite lead octahedron surface are improved after Cl doping. As shown in Figure S4a (Supporting Information), the peak centered at 401 eV is assigned to the N 1s signals of PDA2+ cation. There is a weak extra peak centered at 399.3 eV, which can be attributed to the interaction of Columbic force between the –N+ and perovskite.[24,25] After Cl doping, the intensity of the extra peak is dramatically increased and shifts to higher binding energies of 400.3 eV, as shown in Figure S4 (Supporting Information), suggesting a stronger interaction between the –N+ and perovskite. Due to the interface between the perovskite precursor and PEDOT: PSS provides heterogeneous nucleation sites, the grain nucleates upward from the interface to form perovskites.[26,27] Therefore, Cl doping promotes the interaction between the PDA2+ cations and perovskite to form the graded bandgaps. Otherwise, without Cl doping, the weak interaction between the PDA2+ cations and perovskite leads to accumulation of PDA2+ cations in the top layer during the DMSO solvent evaporation process. Moreover, the presence of PbCl2 can stabilize the precursor phase and slow down the crystallization process of the perovskite.[21] On the other hand, the DMSO[28] and low temperature annealing process are used to slow down the growth rate of perovskite crystal to allow the self-regulation of the reduced-dimensional perovskite to form the quasi-2D perovskite film with vertically graded bandgap, the schematic formation process is shown in Figure 1a. The high angle annular dark field cryo-STEM image of the perovskite film with Cl doping is obtained, as shown in Figure 1c. The C k edge and N k edge

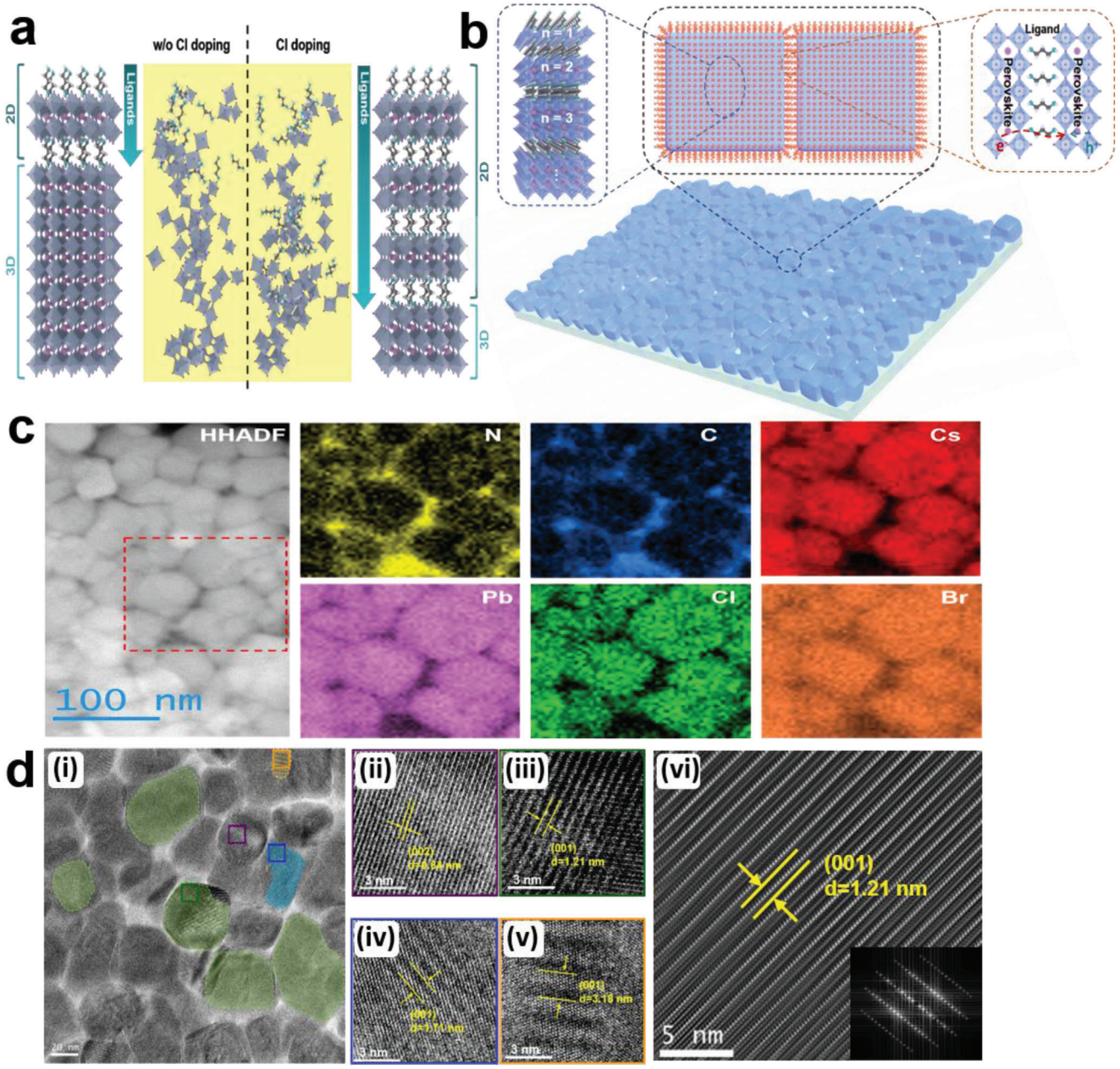

Figure 1. The perovskite films with vertically graded bandgap and grain boundary organic shells. a) The schematic formation process of perovskite films with and without Cl doping. The distribution depth of organic ligands can be prolonged after doping Cl. b) The schematic of the perovskite films with vertically graded bandgap and grain boundary organic shells. c) The cryo-STEM images and low dose cryo-EELS mapping of the perovskite film ($PbCl_2$: $PbBr_2$ = 0.6: 0.4) shown the distribution of different elements. d) The low dose cryo-HRTEM images of different *n* value phases of the perovskite film. i) The magnified TEM images of the perovskite film; The HRTEM images revealed the quasi-2D perovskite different lattice spacings ii) 6.4 Å, iii) 12.1 Å, iv) 17.1 Å, and v) 31.8 Å; vi) the FFT image of the 2D perovskite with inter-planar distance of 12.1 Å.

cryogenic electron energy-loss spectroscopy (cryo-EELS) elemental mapping confirms the formation of an organic shell structure in the grain boundaries. The trap state density estimation demonstrates the organic shell reduces defects, as shown in Figure S5 (Supporting Information). Improving perovskite material quality such as minimizing bulk, surface, and interface defects to reduce the non-radiative recombination rate is a common approach to increase photoluminescence quantum yields (PLQY). Usually, Cl doping causes more defects in the perovskite film, leading to a lower PLQY. However, in this work, the PLQYs can be increased from 57.1% to 76.9% after the molar ratio of PbCl2 to PbBr2 increases to 0.6:0.4, as shown in Figure S6a (Supporting Information). We attribute the higher PLQY to the fact that the organic shells passivate the surface defects. The corresponding photoluminescence (PL) spectra of perovskite film with different PbCl2: PbBr2 molar ratios are shown in Figure S6b (Supporting

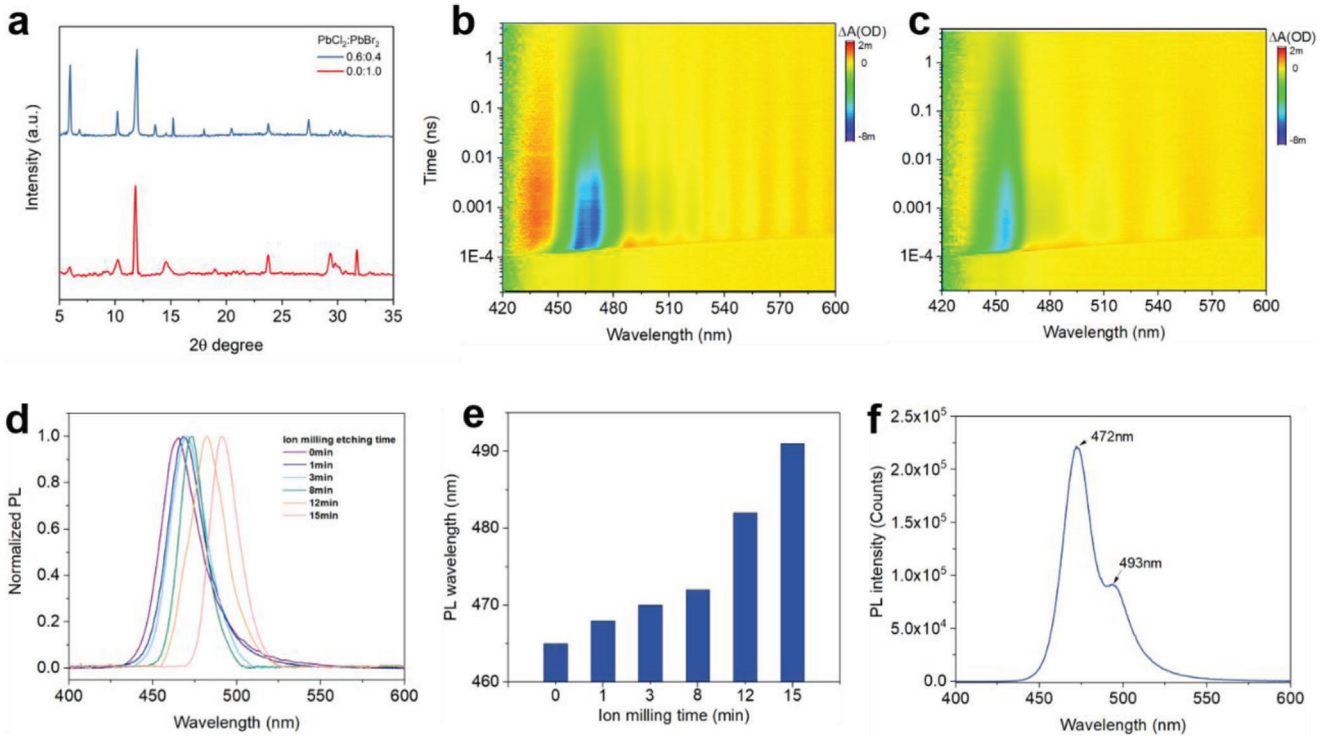

Figure 2. The characterization of perovskite film. a) X-ray diffraction (XRD) patterns of the perovskite film with different $PbCl_2$ to $PbBr_2$ molar ratios. b) Contour plots of the TA spectra of the perovskite film without Cl doping. c) Contour plots of the TA spectra of the perovskite film with Cl doping ($PbCl_2$: $PbBr_2$ = 0.6: 0.4). d) The normalized PL spectra of the perovskite film with $PbCl_2$: $PbBr_2$ = 0.6: 0.4 ratio with varying ion milling time (sample excited from airside). e) The EL peak position of the perovskite with varying ion milling time. f) The PL spectra of the perovskite film excited from the glass side.

Information). The UV–vis absorption spectra of the perovskite film with different PbCl2 concentrations are shown in Figure S7 (Supporting Information). Furthermore, the time-resolved photoluminescence (TRPL) spectra in Figure S8b (Supporting Information) show that perovskite films with organic shells have a longer radiative lifetime than that of the pure Br perovskite film. The longer lifetime of photoluminescence transition is a direct evidence of reduced defects.[9,29] which indicates the passivation of the surface by organic shells. Moreover, the perovskite precursor solution shows no PL emission (Figure S9, Supporting Information) under ultraviolet light, and the TEM images (Figure S10, Supporting Information) of the dropped perovskite precursor solution after annealing also shows no sign of CsPbBrxCl3-x NCs. These results confirm that there are no CsPbBrxCl3-x NCs formed in the perovskite film.

To further verify the existence of different n phases and their distribution trend, cryogenic high resolution transmission electron microscopy (cryo-HRTEM) of the perovskite film is obtained, as shown in Figure 1d and Figure S11 (Supporting Information). The quasi-2D perovskite with different lattice spacing, such as ii) 6.4 Å, iii) 12.1 Å, iv) 17.1 Å, and v) 31.8 Å, are shown in Figure 1d. In addition, the Fast-Fourier transforms (FFT) image of the 2D perovskite with inter-planar distance of 12.1 Å proves the formation of quasi-2D perovskite film, as shown in **Figure 2e-vi**. Furthermore, the TEM images of the graded n value phases distribution at the cross-section part of the perovskite film, as shown in Figure S11 (Supporting Information), demonstrate the vertical distribution trend of the perovskite phase. In the upper layer, HRTEM shows the smallest lattice spacing of 3.04 Å, which corresponds to $n = 1$. For the middle layer, the lattice fringes show a periodicity of 6.04 Å which is about two times of 3.04 Å, thus indicating $n = 2$ in this region. And at the lower part of the film, the lattice fringes with a periodicity of 12.1 Å can be seen, revealing existence of quasi-2D perovskite with $n = 4$ in this region. These results clearly verify that the formation of perovskite films with vertically graded bandgaps.

The X-ray diffraction (XRD) measurement is performed to study the crystal structural property of the perovskite films. According to Figure 2a, the diffraction peaks at 5.89°, 10.3°, and 11.8° are attributed to the formation of quasi-2D perovskite. After introducing $PbCl_2$ into $PDACs_{n-1}Pb_nBr_{3n+1}$ perovskite ($PbCl_2$: $PbBr_2$ = 0.6: 0.4 molar ratio), the new diffraction peaks at 6.8° and 13.6° appear. This suggests that the introduction of $PbCl_2$ affects the distribution of the low-dimensional quasi-2D perovskite in the film. Transient absorption (TA) measurements are conducted to investigate the kinetics of photo-carriers of the perovskite film with pure Br and Cl doping ($PbCl_2$: $PbBr_2$ = 0.6: 0.4 molar ratio). As shown in Figure 2b and Figure S12a (Supporting Information), for pure Br perovskite film, there are two ground-state photo-bleaching signals at 461 and 466 nm from the two-dimensional contour mapping, and the signals of low dimensional phases decrease as the decay time increase in the TA spectra. Meanwhile, multiple signals for large n phases are located at 494, 508, and 523 nm. However, after doping Cl into the

perovskite film, as shown in Figure 2c and Figure S12a (Supporting Information), only a dominant signal at 455 nm is obtained. With the increase in decay time, the signals of low dimensional phases decrease, and there is no obvious photo-bleaching peak of large *n* phase appearing in the TA spectra. This illustrates that doping Cl can thwart the formation of high *n* phase in perovskite film.

To further examining the distribution of quasi-2D perovskites in the film, a systematic investigation on the PL spectra of perovskite thin film at different depths is conducted. Figure 2d presents the normalized PL spectra of the perovskite film with $PbCl_2$: $PbBr_2$ = 0.6: 0.4 molar ratio on ITO/PEDOT: PSS substrate after argon ion milling to remove the surface material in a layer-by-layer fashion (details can be found in Experimental Section). By using this method, the perovskite film can be thinned down layer by layer with high controllability using argon ion milling process and thus the optical properties of the perovskite film at different depths can be investigated. Specifically, we acquired PL spectra by exciting the perovskite film from the upper surface using excitation wavelength of 350 nm, with the results shown in Figure 2e. Before the ion milling process, the PL peak is centered at 465 nm (E_g = 2.62 eV). When the ion milling time increases, the PL peak red-shifts and eventually reaches 491 nm with 15 min ion milling time. These results indicate that after spin coating perovskite on glass/PEDOT: PSS substrate, the upper layer of the film has small *n* number while the lower layer close to the PEDOT: PSS interface has larger *n* number. The trend of gradual redshift when moving toward the PEDOT: PSS/glass substrate suggests that a vertically graded bandgap structure has been formed within the perovskite film. Intriguingly, we discover that the PL spectra appear to have long wavelength emission tail for the film before ion milling and after short ion milling time (<12 min), as shown in Figure S13 (Supporting Information). Especially for the PL acquired after 8 min ion milling (Figure S14, Supporting Information), there is a shoulder peak appearing at 491 nm with the main emission peak positioned at 472 nm. This suggests that the long wavelength PL emission from the bottom of the film with large *n* number quasi-2D perovskite can also show up when the film is thinned down to a proper thickness. To further verify this, we have excited PL of the perovskite film with 8 min ion milling from the glass substrate side. In this case, the bottom of the perovskite film is exposed to excitation source. As shown in Figure 2f, interestingly, the 493 nm emission peak is much more obvious now. This confirms that the large *n* number quasi-2D perovskite PL emission is formed at the bottom of the perovskite film. Meanwhile, the 472 nm emission peak still has significantly higher intensity than the 493 nm peak. This can be rationalized by considering the charge transfer into PEDOT: PSS and the resulting PL quenching effect for the large *n* number quasi-2D perovskite which is adjacent to PEDOT: PSS.

To further prove the formation of perovskite film with vertical graded bandgap structure, the modulation of the recombination zone positions has been conducted. Since our above PL results have shown that the upper layer of the perovskite film has E_g = 2.62 eV (465 nm emission) and the lower layer of the perovskite film possesses E_g = 2.48 eV (491 nm emission), in principle, deep blue to sky blue color EL emission can be achieved via controlling the carrier recombination zone from the upper layer to lower layer of the quasi-2D perovskite film with graded bandgap. Intriguingly, this has been successfully implemented in our work via systematically tuning the thicknesses of ETL and HTL, and the results are shown and discussed below. **Figure 3**a shows the schematic of the EL device architecture with indium-doped tin oxide (ITO)/PEDOT: PSS/perovskite/TPBi/lithium fluoride (LiF)/aluminum (Al) from the bottom to top. The flat-band energy level diagram is shown in Figure S15 (Supporting Information). The valance band position of the perovskite film is determined from the ultraviolet photoelectron spectroscopy (UPS) (Figure S16, Supporting Information), and the E_v of perovskite film with $PbCl_2$: $PbBr_2$ = 0.6: 0.4 molar ratio is −5.97 eV. In addition, the cutoff energy of the perovskite film is gradually increased with the increase of the $PbCl_2$ concentration. We discovered that the recombination zone position in the perovskite film can be rationally controlled by tuning the thicknesses of the HTL or ETL. As shown in the schematic diagram of Figure 3b, the position of the recombination zone descends gradually from the TPBi/perovskite interface to the perovskite/PEDOT: PSS interface when increasing PEDOT: PSS thickness or decreasing the TPBi thickness. According to this scenario, carriers recombine at different depths can generate different EL wavelengths. To verify this hypothesis, we performed a systematic experiment as follows.

Firstly, the TPBi layer thickness is fixed at 50 nm to study the impact of PEDOT: PSS thickness on the device performance. The normalized device EL spectra for different PEDOT: PSS thicknesses varying from 38 to 48 nm are shown in Figure S17 (Supporting Information). The thickness of PEDOT: PSS is controlled by the spin-coating condition and is characterized by an ellipsometer. As the holes are injected from the PEDOT: PSS side, increasing its thickness slows down hole injection and consequently the electron–hole recombination zone moves toward the PEDOT: PSS/perovskite interface. It is worth noting that this recombination zone tuning approach has also been reported previously.[20] As PEDOT: PSS thickness is increased, the EL peak is red-shifted from 469 to 484 nm correspondingly displaying a monotonic trend, as shown in Figure 3c. This confirms that the perovskite film has a vertically graded bandgap structure inside. As shown in Figure 3d, the maximum EQE of the devices with various thicknesses of PEDOT: PSS are achieved. The peak EQE of 9.3% is obtained for the device with 42 nm PEDOT: PSS, which can be attributed to the charge injection balance with the optimal HTL thickness. The corresponding *J*–*L*–*V* curves of the devices with different PEDOT: PSS thicknesses are given in Figure S18 (Supporting Information).

Likewise, it is also observed that the recombination zone position can be tuned by changing the TPBi thickness. In this case, the PEDOT: PSS thickness is fixed at 48 nm and TPBi thickness is systematically increased from 14 to 50 nm. The thickness of TPBi can be well controlled in the evaporation process (Experimental Section). As shown in Figure 3c, an overall blue shift of EL peak position (from 471 to 461 nm) is observed when increasing the TPBi thickness from 14 to 50 nm (in Figure S19, Supporting Information). This can be rationalized by considering the fact that thickening TPBi slows down electron injection thus moving the electron–hole recombination zone toward the perovskite/TPBi interface. Due to the existence of low-*n* dimensional domains (larger bandgap) near the perovskite/TPBi interface, a shorter EL emission wavelength is obtained. The maximum EQE

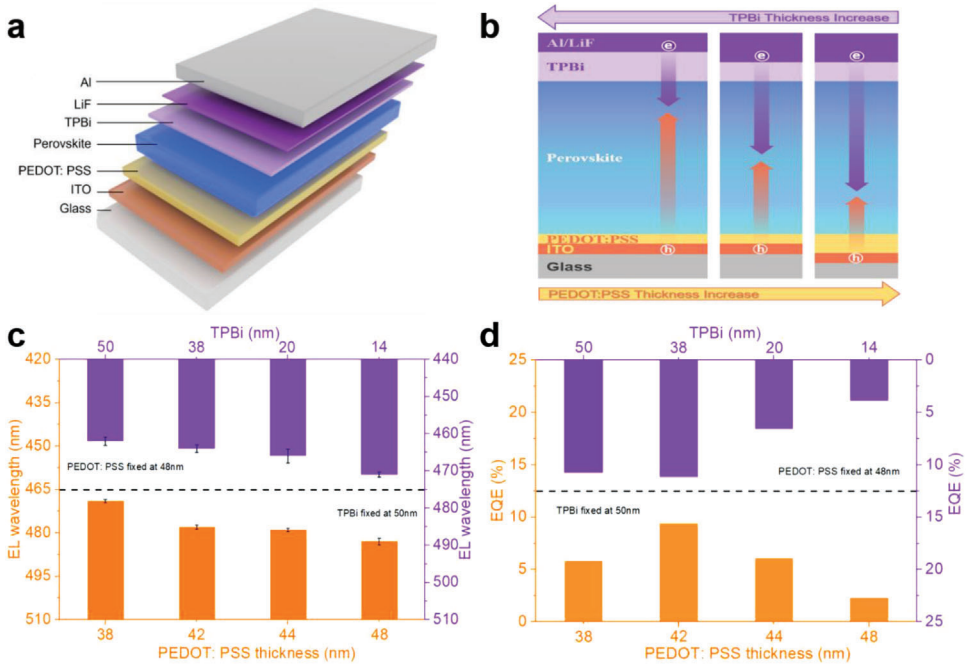

Figure 3. The modulation of recombination zone position within the perovskite emitting layer. a) The device architecture. b) The schematic diagram showing that through tuning the thicknesses of TPBi and PEDOT: PSS, the recombination zone position can be vertically shifted in emitting perovskite layer, therefore varying emission wavelengths can be obtained. c) EL wavelengths of the devices with varying PEDOT: PSS and TPBi thicknesses. The error bars are calculated from ≈5 devices. d) The maximum EQE of the devices varying PEDOT: PSS and TPBi thicknesses.

of devices with various TPBi thicknesses are also achieved, as shown in Figure 3d. The corresponding *J*–*V*–*L* curves of the devices with different TPBi thicknesses are shown in Figure S20 (Supporting Information). Notably, the EQE of the device with 50 nm TPBi reaches ≈10.8% with a deep blue (461 nm) emission, which greatly exceeds that of previously reported deep blue PeLEDs. The corresponding luminance versus EQE curve of the device with 461 nm emission wavelength is shown in Figure S21 (Supporting Information). While tuning the thicknesses of TPBi and PEDOT: PSS, various EL peak positions are obtained due to the fact that the recombination zone position can be modulated to different depths in the quasi-2D perovskite film. These results clearly substantiate the formation of perovskite film with vertically graded bandgap. On the other hand, the vertically graded Br/Cl ratio decreases from top to bottom (as shown in Figure S1b, Supporting Information), which means the bandgap should increase from the top to bottom of the film (more Cl means larger bandgap). However, the PL (Figure 2d–f) and EL (Figure 3c) results show emission peak red shift with longer ion milling etching. This suggests that in reality the bandgap of the perovskite film decreases from the top to bottom of the film. This is opposite to the Br/Cl ratio result. Therefore, we affirm that the vertically graded bandgap is attributed to the graded distribution of n phases.

The wavelength tunable blue PeLEDs with high EQE can be achieved based on the quasi-2D perovskite film with vertically graded bandgap and organic grain boundary passivation shells by optimizing the recombination zone position. The champion device is achieved with optimal TPBi (≈30 nm) and PEDOT: PSS (≈42 nm) thicknesses. The cross-sectional high angle annular dark field scanning transmission electron microscopy (HAADF-STEM) image of the device is shown in **Figure 4**a. The EL result of this device structure is shown in Figure 4b, demonstrating the symmetric pure blue EL spectrum with a peak position located at about 472 nm and a narrow full width at half-maximum (FWHM) of 25 nm. The corresponding Commission International de l'Eclairage (CIE) color coordinate is (0.1303, 0.1124) (Figure S22, Supporting Information), demonstrating the high color purity of blue PeLEDs. Figure 4c shows the current density (*J*)–luminance (*L*)–voltage (*V*) curves of the champion blue PeLEDs with a maximum brightness of 941 cd m^{-2}. The device's peak EQE is 17.5%, as shown in Figure 4d, corresponding to a high current efficiency of ≈19.8 cd A^{-1}. The luminance versus EQE curve is shown in Figure S23 (Supporting Information). After the optimization of the thicknesses of TPBi and PEDOT: PSS, the EQE of 18 devices are shown in Figure 4d. The EL spectra upon various biases are shown in Figure S24 (Supporting Information). To the best of our knowledge, this is the highest EQE for pure and deep blue PeLEDs reported so far. Figure 4f shows the benchmark of our device performance with the existing literature. It can be seen that the unique graded bandgap quasi-2D perovskite film structure has significantly elevated the record EQEs of PeLEDs with pure blue and deep blue emission. Moreover, T50 of the device with an initial brightness of 100 cd m^{-2} is measured as 11.3 min, as shown in Figure S25 (Supporting Information). which is among the longest for the pure and deep blue PeLEDs (Table S1, Supporting Information).

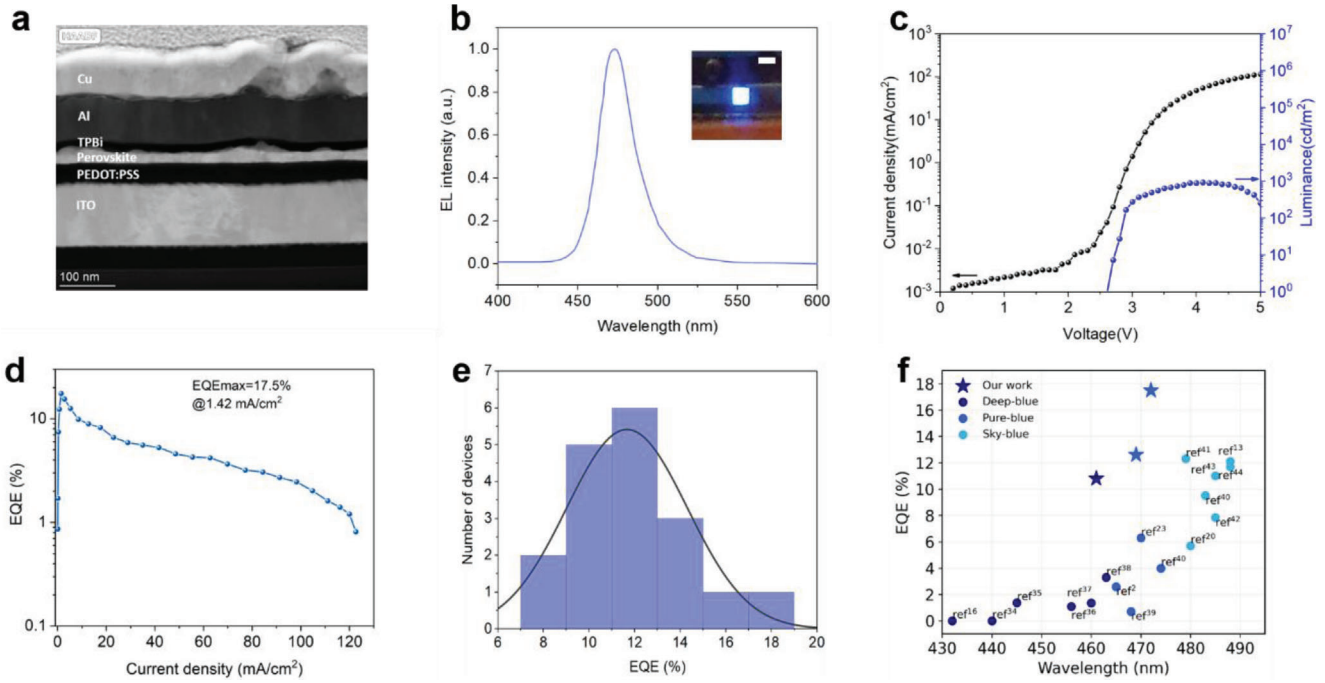

Figure 4. The performance of pure blue PeLEDs. a) The cross-sectional HAADF-STEM image of the device. b) EL spectrum under forward bias. Inset is a photograph of a working blue PeLEDs device (device area ≈ 2.25 mm^2), the scale bar is 1.5 mm. c) Current density–luminance–voltage (*J*–*L*–*V*) curve. d) EQE-*J* curve of the champion device, the peak EQE is 17.5% (1.42 mA cm^{-2}). e) The histogram of EQEs from 18 devices with the optimized PEDOT: PSS and TPBi thicknesses. f) Comparison of our work with recently reported blue perovskite LEDs with emissions in the range from deep blue to sky blue.

3. Conclusion

In this work, we have demonstrated pure and deep blue PeLEDs based on a uniquely designed perovskite film with vertically graded bandgaps and organic grain boundary passivation shells, achieving a high EQE of 17.5% and 10.8% for emission wavelengths of 472 and 461 nm, respectively. The doping of Cl results in the graded distribution of organic ligand (PDA^{2+}) in the perovskite film to form the perovskite film with vertically graded bandgaps and grain boundary organic shells. At the same time, by controlling the thicknesses of hole and electron injection layers to change the position of the recombination zone, the blue emission wavelength of the devices based on the same perovskite materials can be tuned from 461 to 484 nm. Overall, the unique graded bandgap quasi-2D perovskite thin film structure developed here, heralds a new vista to achieve deep and pure blue PeLEDs with high efficiency. And the charge injection tunability demonstrated here can potentially be harnessed for tunable color PeLEDs in broad applications for lighting and display applications in the future.

4. Experimental Section

Materials: Poly(3,4-ethylenedioxythiophene) polystyrene sulfonate (PEDOT: PSS) (AI 4083) was purchased from Ossila. All the other chemicals, CsBr, $PbBr_2$, $PbCl_2$, $PDABr_2$, TPBi, LiF, dimethyl sulfoxide (DMSO) was purchased from Sigma-Aldrich and used as received without further purification.

Perovskite Precursor Solution Preparation: The perovskite precursor solution was prepared by dissolving $PDABr_2$, CsBr, $PbBr_2$, and $PbCl_2$ in DMSO (2 mL), with the molar ratio of $PDABr_2$: CsBr: ($PbBr_2$+$PbCl_2$) equal to 0.169 mmol: 0.308 mmol: 0.308 mmol. The concentrations of $PbCl_2$ (molar ratio of $PbBr_2$: $PbCl_2$ equal to 0.6: 0.4) were introduced into the perovskite precursor solutions. The perovskite precursor solutions were heated and stirred at 75 °C for 2 h and then the solution was subjected to continuous overnight stirring. All the above experiments pertaining to the solution preparation were done in ambient air condition.

Blue PeLEDs Fabrication: The patterned ITO-coated glass substrates were sequentially sonicated with deionized water, isopropyl alcohol, acetone, and then blown dry by nitrogen. ITO glass substrates were treated with oxygen plasma with a power of 100 W for 15 min. Then the PEDOT: PSS (AI 4083) hole transporting layer was prepared by spin-coating PEDOT: PSS aqueous solution onto the ITO substrate at 3600 rpm for 1 min and then baked at 155 °C for 20 min in ambient air. By tuning the spin-coating rates, the thickness of PEDOT: PSS can be adjusted. Then the perovskite precursor solution was spin-coated onto the PEDOT: PSS film at 5000 rpm for 1 min and then annealed at 85 °C for 10 min. The electron transport layer of TPBi was deposited on the perovskite film by using thermal evaporation with a 0.2 nm s^{-1} rate under a vacuum of $<4 \times 10^{-4}$ Pa, and different thicknesses of TPBi were deposited. Finally, 1 nm LiF and 100 nm Al were deposited using the same evaporation system. The overlapping area of ITO and Al electrodes was the device area (≈2.25 mm^2).

Characterization: Field-emission scanning electron microscopy (JEOL JSM-7800F) was used to characterize the top-view morphology of the perovskite film with different $PbCl_2$ concentrations. The PL, PLQY, and TRPL were performed with Edinburgh Instruments FLS920P. For the ion milling etching process, the accelerating voltage was 120 V, and the title angle between the perovskite films and the argon ion beam was about 70–80° during the etching process. The chamber pressure was about 4×10^{-4} Pa and Ar gas flow was 4–12 sccm. A Titan Krios G3i with Cs-aberration corrector operating at 300 kV was used to characterize and prepare samples.

It was fitted with Cs CETCOR/S-CORR image Corrector, Gatan Continuum K3 300 kV (Gatan Continuum 1069, EELS) with Post-GIF Gatan K3 Summit (5760 × 4092) direct detection camera as a detector. The cryo-EELS maps were acquired using 17 pA current with 0.05 s dwell time at each pixel. For cryo-high resolution (HR)-TEM image, the prepared FIB lamina was then immediately dropped in liquid nitrogen and transferred by a cryo-autoloader into cryogenic chamber of Titan Krios cryo-TEM (Thermo Fisher Scientific Ltd.). The cryo-TEM images were acquired using a low electron dose detector (Falcon IV direct detection camera, Thermo Fisher Scientific Ltd.). The cryo-HRTEM images were acquired at liquid N_2 with an electron dose rate ≈5.8 e Å^{-2} s^{-1} for ≈5 s. And the TEM model of JEM-ARF200F (JEOL) was used. The TEM sample was prepared by cross sectional cutting, lifted off and attached with the help of dual beam FIB. The final thinning voltage used was 2 kV and the lamella thickness was less than 100 nm. The Transient absorption measurements were conducted by using a regeneratively amplified Ti:sapphire laser source (Coherent Legend, 800 nm, 150 fs, 5 mJ per pulse, and 1 kHz repetition rate) and Helios (Ultrafast Systems LLC) spectrometers. The atom concentration was measured by Kratos X-ray photoelectron spectrometer (Axis Ultra DLD by Kratos). The sputtering conditions: Ar, 4 kV, 3 × 3 mm raster, 140 µA extractor current. The performance of blue PeLEDs was measured by using a source-measurement-unit Keithley 2400 and a spectrometer (Ocean Optics, Flame-S-VIS-NIR-ES). The *J–V* data from 0 to 5 V were measured, the scan step voltage was 0.1 V with delay time 1 s, and the integral time was 100 ms. The XRD spectra of the perovskite films were measured on a Rigaku Smart Lab (λ = 1.54 Å).

Supporting Information

Supporting Information is available from the Wiley Online Library or from the author.

Acknowledgements

This work was financially supported by Hong Kong Research Grant Council (General Research Fund Project Nos. 16214619, 16205321, 16309018), Hong Kong Innovation Technology Fund (GHP/014/19SZ), HKUST Fund of Nanhai (Grant No. FSNH-18FYTRI01), Guangdong-Hong Kong-Macao Intelligent Micro-Nano Optoelectronic Technology Joint Laboratory (Project No. 2020B1212030010), Foshan Innovative and Entrepreneurial Research Team Program (2018IT100031), The Fundamental and Applied Research Grant of Guangdong Province (2021A1515110627), and Southern University of Science and Technology Grant (Y01796108). The authors also acknowledge the support from the State Key Laboratory of Advanced Displays and Optoelectronics Technologies at HKUST. The authors would like to acknowledge the technical support from SUSTech CRF. They thank Y. Zhu for assistance with the SEM measurement, B. Ren, Z. Ma, C. L. J. Chan, C. Wang, and X. Qiu for assistance with the data analysis, M. Qin for assistance with the XRD measurements.

Conflict of Interest

The authors declare no conflict of interest.

Author Contributions

Z.F. and L.S. conceived the idea and designed the experiments. Z.F. supervised the work. L.S., Q.Z., and Z.F. wrote the manuscript and did the data analysis. L.S. and S.P. carried out the TEM measurement and FIB cutting. L.S., Q.Z., D.Z., Y.F., and B.C. carried out the device fabrication and characterizations. Y.D. participated in data analysis and paper revision. All authors contribute to the paper discussion and agree with the results. L.S. and B.H. contributed equally to this work.

Data Availability Statement

The data that support the findings of this study are available from the corresponding author upon reasonable request.

Keywords

quasi-2D perovskite materials, pure and Deep blue PeLEDs, wavelength tunable

Received: August 1, 2023
Published online:

[1] S. Yuan, Z. K. Wang, L. X. Xiao, C. F. Zhang, S. Y. Yang, B. B. Chen, H. T. Ge, Q. S. Tian, Y. Jin, L. S. Liao, *Adv. Mater.* **2019**, *31*, 1904319.
[2] Y. Jiang, C. Qin, M. Cui, T. He, K. Liu, Y. Huang, M. Luo, L. Zhang, H. Xu, S. Li, J. Wei, Z. Liu, H. Wang, G. H. Kim, M. Yuan, J. Chen, *Nat. Commun.* **2019**, *10*, 1868.
[3] Y. H. Kim, S. Kim, A. Kakekhani, J. Park, J. Park, Y. H. Lee, H. Xu, S. Nagane, R. B. Wexler, D. H. Kim, S. H. Jo, L. Martínez-Sarti, P. Tan, A. Sadhanala, G. S. Park, Y. W. Kim, B. Hu, H. J. Bolink, S. Yoo, R. H. Friend, A. M. Rappe, T. W. Lee, *Nat. Photonics* **2021**, *15*, 148.
[4] Y. Hassan, J. H. Park, M. L. Crawford, A. Sadhanala, J. Lee, J. C. Sadighian, E. Mosconi, R. Shivanna, E. Radicchi, M. Jeong, C. Yang, H. Choi, S. H. Park, M. H. Song, F. De Angelis, C. Y. Wong, R. H. Friend, B. R. Lee, H. J. Snaith, *Nature* **2021**, *591*, 72.
[5] K. Lin, J. Xing, L. N. Quan, F. P. G. de Arquer, X. Gong, J. Lu, L. Xie, W. Zhao, D. Zhang, C. Yan, W. Li, X. Liu, Y. Lu, J. Kirman, E. H. Sargent, Q. Xiong, Z. Wei, *Nature* **2018**, *562*, 245.
[6] Y. Cao, N. Wang, H. Tian, J. Guo, Y. Wei, H. Chen, Y. Miao, W. Zou, K. Pan, Y. He, H. Cao, Y. Ke, M. Xu, Y. Wang, M. Yang, K. Du, Z. Fu, D. Kong, D. Dai, Y. Jin, G. Li, H. Li, Q. Peng, J. Wang, W. Huang, *Nature* **2018**, *562*, 249.
[7] T. Chiba, Y. Hayashi, H. Ebe, K. Hoshi, J. Sato, S. Sato, Y. J. Pu, S. Ohisa, J. Kido, *Nat. Photonics* **2018**, *12*, 681.
[8] W. Xu, Q. Hu, S. Bai, C. Bao, Y. Miao, Z. Yuan, T. Borzda, A. J. Barker, E. Tyukalova, Z. Hu, M. Kawecki, H. Wang, Z. Yan, X. Liu, X. Shi, K. Uvdal, M. Fahlman, W. Zhang, M. Duchamp, J. M. Liu, A. Petrozza, J. Wang, L. M. Liu, W. Huang, F. Gao, *Nat. Photonics* **2019**, *13*, 418.
[9] Z. Chu, Y. Zhao, F. Ma, C. X. Zhang, H. Deng, F. Gao, Q. Ye, J. Meng, Z. Yin, X. Zhang, J. You, *Nat. Commun.* **2020**, *11*, 4165.
[10] M. Karlsson, Z. Yi, S. Reichert, X. Luo, W. Lin, Z. Zhang, C. Bao, R. Zhang, S. Bai, G. Zheng, P. Teng, L. Duan, Y. Lu, K. Zheng, T. Pullerits, C. Deibel, W. Xu, R. Friend, F. Gao, *Nat. Commun.* **2021**, *12*, 361.
[11] H. Zhang, X. Fu, Y. Tang, H. Wang, C. Zhang, W. W. Yu, X. Wang, Y. Zhang, M. Xiao, *Nat. Commun.* **2019**, *10*, 1088.
[12] S. Kumar, J. Jagielski, S. Yakunin, P. Rice, Y. C. Chiu, M. Wang, G. Nedelcu, Y. Kim, S. Lin, E. J. G. Santos, M. V. Kovalenko, C. J. Shih, *ACS Nano* **2016**, *10*, 9720.
[13] P. Vashishtha, M. Ng, S. B. Shivarudraiah, J. E. Halpert, *Chem. Mater.* **2019**, *31*, 83.
[14] J. Xing, Y. Zhao, M. Askerka, L. N. Quan, H. Tan, G. Long, L. Gao, Z. Yang, Z. Lu, Q. Xiong, E. H. Sargent, X. Gong, W. Zhao, J. Zhao, O. Voznyy, J. Tang, *Nat. Commun.* **2018**, *9*, 3541.
[15] M. Yuan, L. N. Quan, R. Comin, G. Walters, R. Sabatini, O. Voznyy, S. Hoogland, Y. Zhao, E. M. Beauregard, P. Kanjanaboos, Z. Lu, D. H. Kim, E. H. Sargent, *Nat. Nanotechnol.* **2016**, *11*, 872.
[16] Z. Li, Z. Chen, Y. Yang, Q. Xue, H. L. Yip, Y. Cao, *Nat. Commun.* **2019**, *10*, 1027.
[17] K. H. Stone, A. Gold-Parker, V. L. Pool, E. L. Unger, A. R. Bowring, M. D. McGehee, M. F. Toney, C. J. Tassone, *Nat. Commun.* **2018**, *9*, 3458.

[18] L. Cheng, T. Jiang, Y. Cao, C. Yi, N. Wang, W. Huang, J. Wang, *Adv. Mater.* **2020**, *32*, 1904163.
[19] R. Quintero-Bermudez, A. Gold-Parker, A. H. Proppe, R. Munir, Z. Yang, S. O. Kelley, A. Amassian, M. F. Toney, E. H. Sargent, *Nat. Mater.* **2018**, *17*, 900.
[20] D. Shen, Z. Ren, Q. Li, C. Luo, W. Xia, Z. Zheng, W. Ma, J. Li, Y. Chen, *ACS Appl. Mater. Interfaces* **2022**, *14*, 21636.
[21] J. Song, J. Li, L. Xu, J. Li, F. Zhang, B. Han, Q. Shan, H. Zeng, *Adv. Mater.* **2018**, *30*, 1805409.
[22] Y. Yu, S. Yang, L. Lei, Y. Liu, *Nanoscale* **2017**, *9*, 2569.
[23] J. W. Lee, D. K. Lee, D. N. Jeong, N. G. Park, *Adv. Funct. Mater.* **2019**, *29*, 1807047.
[24] M. Zhou, C. Fei, J. S. Sarmiento, H. Wang, *Sol. RRL* **2019**, *3*, 1970111.
[25] W. S. Yang, B. W. Park, E. H. Jung, N. J. Jeon, Y. C. Kim, D. U. Lee, S. S. Shin, J. Seo, E. K. Kim, J. H. Noh, S. Il Seok, *Science* **2017**, *356*, 1376.
[26] X. Yang, X. Zhang, J. Deng, Z. Chu, Q. Jiang, J. Meng, P. Wang, L. Zhang, Z. Yin, J. You, *Nat. Commun.* **2018**, *9*, 2.
[27] Z. Chen, M. Liu, Z. Li, T. Shi, Y. Yang, H. L. Yip, Y. Cao, *iScience* **2018**, *9*, 337.
[28] G. Yang, X. Liu, Y. Sun, C. Teng, Y. Wang, S. Zhang, H. Zhou, *Nanoscale* **2020**, *12*, 1571.
[29] Q. Zhang, M. M. Tavakoli, L. Gu, D. Zhang, L. Tang, Y. Gao, J. Guo, Y. Lin, S. F. Leung, S. Poddar, Y. Fu, Z. Fan, *Nat. Commun.* **2019**, *10*, 727.